UNIVERSIDAD DE CONCEPCIÓN
FACULTAD DE CIENCIAS FÍSICAS Y MATEMÁTICAS

Modeling of Archean Earth-like aquaplanets atmospheres: the effect of obliquity on habitability and observables of exoplanets

Modelamiento de atmósferas de aquaplanets similares a la Tierra Arcaica: el efecto de la oblicuidad en la habitabilidad y observables de exoplanetas

Benji S. E. González-Vidal
Coautorx: Aurora Lagos-Duarte, Dr. Vincent Kofman, Dr. Ricardo Demarco

Tesis presentada a la Facultad de Ciencias Físicas y Matemáticas
de la Universidad de Concepción para optar al grado académico de
Magíster en Astronomía

Junio 2024
Concepción, Chile

Profesor Guía: Dr. Rodrigo Reeves

A mi Memita Lunar, Madre, Padre, hermanxs y Almita bebé.

AGRADECIMIENTOS

Primero, a mi mamá y papá quienes son el pilar principal de todo lo que soy y hago. A mi hermana Pame, que me enseña a hacer las cosas con amor. A mi hermanito Diego, que me mostró lo interesante que es la física y que siempre está ahí para contener y ayudarme cuando lo necesito. A mi sobrina/hermana Kiara, que me enseña a seguir firme mi camino y a seguir a mi corazón. A mi Luna (Meme), que me acompañó en todos mis procesos y se quedó lo que mas pudo su cuerpita para poder acompañarnos. A mi Almita bb, que me devolvió esa chispa de felicidad y amorcito que había perdido cuando la Memita se fue. Gracias a Kamilla Barra, Ricardo Demarco y el Grupo de AstroGeoBiologia (AGB) por acompañarnos en este camino por la curiosidad de imaginar otros mundos y en la astrobiología. A Marcelo Ramírez , que sin su asistencia técnica y enseñanzas en computación, hubiera sido aun mas difícil la simulación de las atmósferas. A Priscilla Nowajewsky, por acompañar en el inicio de este proyecto. A Programa de Monitoreo Sísmico en tiempo Cuasi-Real, Geología y Geofísica Aplicada al Medioambiente (GEMA). Por facilitar recursos computacionales y asistencia técnica. A Aurora Lagos-Duarte, por ser una compañera excepcional y una persona fundamental en el desarrollo de este trabajo. También por darle sentido a este proyecto y por lo cual me motivaba día a día a seguir trabajando. A Vincent Kofman, por su amabilidad, ayuda desinteresada y su contribución importante en el trabajo. Gracias a ambxs (Aurora y Vincent), por compartir el espíritu de la colaboración abierta. Adiv Paradise, Frank Lukeint, desarrolladores de ExoPlaSim y PlaSim, por su asistencia vía e-mail en la instalación y uso de sus modelos. Raphael Gobat quien ayudo aportando comentarios relevantes para este trabajo. A todas las personas y seres que me han sostenido en este proceso. Agradezco a mi yo de todas las épocas, que ha sido dura pa'l concurso.

Resumen

La búsqueda y observación de exoplanetas habitables similares a la Tierra, así como la interpretación de estas observaciones, se han convertido en temas centrales de la astronomía actual.

Nuestro objetivo es investigar la interacción entre la oblicuidad planetaria, la termodinámica atmosférica y los procesos hidrológicos, y su impacto en la habitabilidad y las propiedades espectroscópicas de los acuaplanetas con una composición atmosférica similar a la de la Tierra Arcaica.

Utilizando un modelo de circulación general (GCM) y modelos de transferencia radiativa (RT) para simulaciones atmosféricas y de espectros de emisión, modelamos diez acuaplanetas con atmósfera similar a la de la Tierra Arcaica con oblicuidades variables. La habitabilidad se analiza a través de la temperatura de la superficie del mar (T_S) y la temperatura del bulbo húmedo (T_W). Se analiza el espectro de emisión para determinar los cambios debidos al efecto de la oblicuidad.

Nuestros resultados confirman que la oblicuidad influye significativamente en su termodinámica atmosférica, la habitabilidad de la superficie y los espectros de emisión observables para el caso sin nubes. En particular, los rasgos de absorción de vapor de agua de 2.7 y 6.0 μm en escenarios sin nubes se correlacionaron con T_W para oblicuidades mayores o iguales a 52.5^o.

Nuestros hallazgos proporcionan información sobre las posibles características climáticas y espectrales de las atmósferas de tipo Arcaico relacionadas con la oblicuidad, ofreciendo una base para interpretar las observaciones de exoplanetas. Estos resultados podrían servir de base para futuras misiones telescópicas y contribuir al desarrollo de métodos para estimar la oblicuidad y la habitabilidad de exoplanetas a partir de datos espectroscópicos.

Keywords – Atmósferas de exoplanetas, Climas planetarios, Espectroscopia IR, Habitabilidad, Astrobiología

Abstract

The search for and observation of habitable Earth-like exoplanets, as well as the interpretation of these observations, have become central topics in astronomy today.

We aim to investigate the interplay between planetary obliquity, atmospheric thermodynamics, and hydrological processes, and their impact on the habitability and spectroscopic properties of aquaplanets with an Archean Earth-like atmospheric composition.

Using a General Circulation Model (GCM) and radiative transfer (RT) for atmospheric and emission spectra simulations, we modeled ten aquaplanets with Archean Earth-like atmosphere with varying obliquities. Habitability is analyzed through the Sea Surface Temperature (T_S) and the Wet Bulb Temperature (T_W). Emission spectrum is analyzed to determine the changes due to the effect of obliquity.

Our results confirm that the obliquity significantly influences its atmospheric thermodynamics, surface habitability, and observable emission spectra for cloudless case. Notably, the 2.7 and 6.0 μm water vapor absorption features in cloudless scenarios correlated with T_W for obliquities greater than or equal to 52.5^o.

Our findings provide insights into the potential climatic and spectral characteristics of Archean-like atmospheres related with obliquity, offering a basis for interpreting exoplanet observations. These results could inform future telescope missions and aid in the development of methods to estimate exoplanetary obliquity and habitability from spectroscopic data.

Keywords – Exoplanet atmospheres, Planetary climates, Infrared spectroscopy, Habitability, Astrobiology

Contents

List of Tables

List of Figures

Chapter 1

Introduction

Habitability remains a concept challenging to define. Understanding the conditions necessary for habitability and the detection of potential biosignatures are key objectives in exoplanetary sciences (Ozaki et al., 2022). Transmission spectroscopy has enabled detailed studies of exoplanetary atmospheres, providing insights into their potential habitability (Ozaki et al., 2022). Thanks to the Kepler and TESS missions, about 5,000 exoplanets have been detected (Kossakowski et al., 2023), with nearly 50 found orbiting within the Habitable Zone (HZ) — the region where Earth-like planets can sustain liquid water on their surface (Childs et al., 2022; Kasting et al., 1993; Segura et al., 2005). Among these, 20 are considered Earth-like, defined as $0.8R_{\oplus} < R_p < 1.6M_{\oplus}$ and $0.5M_{\oplus} < M \sin i_p < 3M_{\oplus}$ (Kossakowski et al., 2023). However, the mere characterization of atmospheric composition does not definitively indicate a planet's ability to support life (Ozaki et al., 2022). Additional analyses, such as the presence of liquid water, must also be considered (Seager, 2014).

The presence of liquid water is crucial for assessing a planet's potential for habitability (Childs et al., 2022; Kasting et al., 1993). Earth, the only planet known to harbor life, relies on liquid water for its habitability, as it allows the transport of many molecules necessary to form living molecular systems, such as cells (do Nascimento Vieira et al., 2020). If a planet has liquid water, we can presume that Earth-like life forms might inhabit it (Hedelt et al., 2013; Seager, 2014). However, for water to be in liquid phase on the surface, suitable surface temperature and atmospheric pressure are required (Seager, 2014; Carr and Head,

2010; Segura et al., 2005). These factors depend on the spectral type of the host star (Kopparapu et al., 2013; Nowajewski et al., 2018), the chemical composition of the atmosphere, the amount of atmospheric gases, the planet's surface (Kopparapu et al., 2013; Nowajewski et al., 2018), and orbital parameters like eccentricity (Linsenmeier et al., 2015) and obliquity (ϕ; Linsenmeier et al. (2015); Nowajewski et al. (2018)).

To understand the complex interplay between orbital parameters, habitability, and observational characteristics, researchers have turned to atmospheric modeling of exoplanets using General Circulation Models (GCMs) and radiative transfer models to simulate how these planets would appear when observed using transmission spectroscopy (Kopparapu et al., 2017; Fauchez et al., 2019). These models allow for the simulation of Earth-like exoplanets and provide insights into how their potential habitability would manifest in observational data gathered through transmission spectroscopy under various conditions.

Studies, such as Nowajewski et al. (2018), have highlighted the importance of parameters like obliquity in determining the habitability of exoplanets. Experimental simulations of Earth-like aquaplanets with modern atmospheric CO_2 concentration suggest that while surface temperatures (T_S) may support liquid water throughout the year, the atmospheric habitability indicator, Wet Bulb Temperature (T_W), reveals variations in surface habitability across aquaplanets with different obliquities throughout the year. Even if a planet retains liquid water, it does not imply that the atmosphere is suitable for surface life; parameters such as T_W must also be considered (Nowajewski et al., 2018). However, it remains uncertain whether these effects of obliquity on habitability can be observed spectroscopically. This not only enhances our understanding of exoplanet habitability but also provides valuable insights into how observational data can be interpreted.

Understanding the habitability and observational characteristics of exoplanets is crucial, especially when considering Earth-like conditions. However, it's essential to recognize that modern Earth is not the only model of a habitable planet. While much attention has been given to studying exoplanets resembling contemporary Earth, which are primarily composed of N_2 and O_2, it's equally important to explore other potential habitable environments (Arney et al., 2016). During the Archean Eon, approximately $4.3 - 3.0$ billion years ago, life originated in a vastly

different environment compared to present-day Earth (Catling and Zahnle, 2020). The atmospheric composition during this epoch consisted mainly of N_2 and CO_2 (Catling and Zahnle, 2020), and the Sun's luminosity was estimated to be $20-25\%$ lower than today (Catling and Zahnle, 2020; Bahcall et al., 2001), with a radius approximately 9% smaller (Bahcall et al., 2001) and an effective temperature around 1% lower (Bahcall et al., 2001) according to standard solar evolution models. While most studies have focused on considering exoplanets as contemporary Earth-like planets, there is limited exploration of the habitability and observability of exoplanets resembling the Archean Earth. Few studies have considered the combination of Archean-like conditions with an orbital parameter such as obliquity as a modulator of habitability to compare their spectral characteristics. This expands the potential diversity of habitable exoplanets or those suitable for the development of life similar to Earth's (Arney et al., 2016).

In this paper, we aim to address the following scientific question: What are the spectral properties of an Earth-like aquaplanet with different habitability conditions determined by its obliquity, considering the atmospheric composition characteristic of the Archean-Earth?

To address this question, our study investigates the interplay among planetary obliquity, atmospheric thermodynamics, and their impact on the habitability and spectroscopic properties of such an exoplanet.

We hypothesize that the obliquity of an Archean-Earth-like aquaplanet with the atmospheric composition of the Archean-Earth directly influences its atmospheric thermodynamics, thereby impacting surface habitability with the presence of surface liquid water and atmospheric moisture, observable through spectroscopy.

Chapter 2

Methodology

This work is divided into two parts: an Atmospheric Simulation using a General Circulation Model (GCM) and the Spectra Simulation using a Radiative Transfer (RT) model to simulate an Earth-like aquaplanet with an atmospheric composition similar to Earth's Archean era, 3.0 billion years ago (Archean-Earth, Catling and Zahnle (2020)).

We simulate 10 aquaplanets with different obliquities using a GCM, and then simulate the emission spectrum of the planet's atmosphere through a radiative transfer model. Habitability is analyzed through the Sea Surface Temperature (T_S) and the Wet Bulb Temperature (T_W) of the aquaplanet to verify if the surface water remains in liquid phase and to assess if it is habitable for Current-Earth-like life forms. Then, the emission spectra are calculated using the variables given by the GCM. The resulting model spectrum is analyzed to determine the changes in the planet's emission spectra due to the effect of obliquity.

2.0.1 Atmospheric Simulation

In our atmospheric simulations, we employ ExoPlaSim (Release 3.3.0; Paradise et al. (2022)) to recreate a Archean-Earth atmosphere. This intermediate-complexity GCM, developed by Paradise et al. (2022), is derived from the GCM Planet Simulator (PlaSim) by Fraedrich et al. (2005) to simulate exoplanet atmospheres. GCMs like ExoPlaSim provide a comprehensive representation of Earth-system components, encompassing the atmosphere, land, ocean, and sea ice. This allows us to efficiently simulate crucial 3D processes, including

cloud formation, large-scale circulation, moist processes, and climate feedbacks, at reduced computational expense. It is important to note that this GCM incorporates certain simplifications through parameterizations of processes, such as radiative transfer and microphysics (Chen et al., 2023).

ExoPlaSim assumes the planet is irradiated by a blackbody with the defined effective temperature of the star. For our simulations, we assume an Earth-like aquaplanet with an atmospheric composition similar to Archean-Earth. We use the Standard Solar Model with the present age of the Sun being 4.57 billion years. The luminosity ($L_\odot$), radius ($R_\odot$), and effective temperature ($T_{eff,\odot}$) of the Sun are $3.844 \times 10^{26}\ W$ (Bahcall et al., 2001), $6.957 \times 10^{8}\ m$, and 5777 K, respectively. The decision to use a contemporaneous Sun in L_{odot}, R_{odot}, and $T_{eff,\odot}$ is based on the fact that if we define those parameters to simulate an Archean Sun, the planets enter into a snowball effect. This problem is known as the faint young Sun paradox, which has been widely discussed (Rondanelli and Lindzen, 2010) and is beyond the scope of our work.

Parameter	**Value**	**Reference**
Radius	$6.957 \times 10^{8}\ m$	Bahcall et al. (2001)
Luminosity	$3.844 \times 10^{26}\ W$	Bahcall et al. (2001)
Temperature	$5777\ K$	Bahcall et al. (2001)

Table 2.0.1: Sun parameters used as input in ExoPlaSim for our Archean Earth-like aquaplanet model.

The aquaplanet has a radius (R) of 6300 km, a mass (M) of 5.9736×10^{24} kg, and a gravity acceleration (g) of 9.8 ms^{-2}. It orbits its star at a distance of 1 AU with zero eccentricity ($\epsilon = 0$) and varying obliquities (ϕ) of $\{0^o, 10^o, 23.5^o, 30^o, 40^o, 52.5^o, 60^o, 70^o, 80^o, 90^o\}$. These obliquities were chosen to sample from 0^o to 90^o. The 23.5^o obliquity value represents current Earth's obliquity for comparison purposes, since the current Earth is a reference point for a lot of studies (Nowajewski et al., 2018). The 52.5^o obliquity case is included as it represents a limit case where the equator-to-pole difference of incoming solar radiation at the top of the atmosphere is zero, resulting in homogeneous average annual insolation (Nowajewski et al., 2018). We replicate the simulation of $\phi = 52.5^o$ to analyze climate behavior under the Archean-Earth model. Months are set to equal lengths of 29 days, and years have 360 days. ExoPlaSim includes sea-ice-atmosphere interaction and a slab ocean with a fixed depth (Paradise et al.,

2022).

Orography is set to zero to ignore zonal asymmetries introduced by factors such as continents and focus on climate responses. Horizontal ocean heat transport is set to zero at all latitudes and longitudes. We assume a slab ocean model with a depth of 50 m. An oceanic albedo of 0.06 (Donohoe and Battisti, 2011) and a sea-ice albedo of 0.75 (Robock, 1980) are adopted.

For the atmosphere, we assume 10 linear vertical levels from 1 bar to 0.1 bar, describing the surface to the lower stratosphere. Given that nitrogen (N_2) is the most abundant molecule in the Archean atmosphere (Catling and Zahnle, 2020), our model assumes an atmosphere composed only of N_2 and carbon dioxide (CO_2). The total atmospheric pressure is assumed to be 1000 hPa, with CO_2 partial pressure taken from Catling and Zahnle (2020) and the rest assumed to be N_2. These two species are assumed to be well mixed. Water vapor (H_2O) and water content in clouds (C_{LW}) vary based on the meteorological conditions computed by the model.

Parameter	**Value**	**Reference**
	Planet	
Radius	1 [Earth radii]	-
Gravity acceleration	9.8 $[ms^{-2}]$	-
Month	29 [days]	Nowajewski et al. (2018)
Day	24 $[h]$	-
	Orbital	
Distance from the Star	1 [AU]	-
Year	360 [days]	-
Eccentricity	0 [°]	Nowajewski et al. (2018)
Obliquity (ϕ)	$0, 10, 23.5, 30, 40, 52.5, 60, 70, 80, 90$ [^{o}]	-
	Atmosphere	
Vertical Discretization	Linear	-
Min/Max Pressure	100 / 1000 $[hPa]$	Nowajewski et al. (2018)
Partial pressures	$N_2 = 0.965$ [bar] $CO_2 = 0.035$ [bar]	Catling and Zahnle (2020)
Ozone	No	-
	Surface	
Aquaplanet	Yes	-
Orography	No	-
Ocean Depth	50 $[m]$	Nowajewski et al. (2018)
Ocean Albedo	0.06	Donohoe and Battisti (2011)
Sea Ice Albedo	0.7	Robock (1980)

Table 2.0.2: Aquaplanet parameters used for our Archean Earth-like model with ExoPlaSim.

ExoPlaSim operates with a spatial resolution of T42 ($2.8° \times 2.8°$), which corresponds to grids of 64 latitudes and 128 longitudes. Each simulation experiment is performed using a computing cluster with 16 cores at 4.5 GHz, covering a period of 150 simulated years. The climatologic average is derived from the final 50 years of simulations, during which the climate of the aquaplanet will be in a stationary state. This climatologic average represents the characteristic climate regime, far from the initial condition imposed.

To achieve this, we analyze the radiative energy flux budget at the Top of the Atmosphere (TOA) for each experiment. When the net energy budget at TOA the is zero, means that the incident energy flux is equal to outgoing energy flux. This analysis help us identify if the simulated aquaplanets have reached an equilibrium state and exclude cases where the planet enters a snowball state or a greenhouse effect.

To compute the energy budget on the TOA, we calculate the global average for net radiative flux at TOA. To compute global averages, we weight each grid with the cosine of latitudes. This is a common practice in GCM studies to calculate meridionally averaged variables (Yang et al., 2024). If the global average of the Net TOA Radiation is near to zero, the climate of the aquaplanet have reached the equilibrium.

2.0.2 Habitability

Once verified that the climate of aquaplanets reached the equilibrium, we analyze the Sea Surface Temperature (T_S) and Wet Bulb Temperature (T_W). The habitable range for T_S is between 273.15 K and 373.15 K to ensure liquid water, and T_W is between 273.15 K and 308.15 K, the habitable range for mammalian life (Nowajewski et al., 2018). Although this range is defined for mammals, various habitable ranges exist for different life forms. Our focus simplifies the problem by defining a single case of interest, but this methodology can apply to other life forms, opening possibilities for future habitability studies.

We compute the T_W using Stull (2011) formula, as in Nowajewski et al. (2018):

$$
\begin{aligned}
T_W = T_A \tan^{-1}\left(0.151977(q + 8.313659)^{1/2}\right) + \tan^{-1}(T_A + q) \\
- \tan^{-1}(q - 1.676331) + 0.00391838q^{3/2} \cdot \tan^{-1}(0.023101q) \\
- 4.686035
\end{aligned}
\tag{2.0.1}
$$

Where T_A is the air temperature and q is relative humidity computed from ExoPlaSim.

2.0.3 Spectral Simulation

The next component of this study is the simulation of synthetic emission spectra for various aquaplanets with different obliquities. This is achieved using a Radiative Transfer Model to generate the spectral data. Specifically, we employ NASA's Planetary Spectrum Generator (PSG, https://psg.gsfc.nasa.gov, Villanueva et al. (2018)) for this purpose.

PSG is an advanced radiative-transfer code developed for the analysis of various celestial bodies within and beyond our solar system (Villanueva et al., 2018). It allows the synthesis of planetary atmospheres and surface spectra across a wide range of wavelengths, from UV to radio frequencies, and supports different observation platforms like observatories, orbiters, and landers (Fauchez et al., 2019). PSG combines multiple sophisticated radiative transfer models, spectroscopic databases, and planetary databases, integrating climatological and orbital data to enhance its computational capabilities (Villanueva et al., 2018). It employs state-of-the-art radiative-transfer and scattering methods to produce high-resolution spectra through line-by-line calculations and uses the correlated-k method for moderate resolution spectra.

In our study, we utilize the parameters provided by ExoPlaSim as inputs to PSG. These parameters include latitudes, longitudes, T_S, T_A , air pressure (P_A), eastward/northward winds (u/v), H_2O, C_{LW}, and albedo. We compute the combined emitted and reflected introducing the ExoPlaSim's simulation variables to the PSG module Global Exoplanetary Spectra (GlobES, Villanueva et al. (2022)) using a "binning" factor of 5. This means that PSG/GLobES performs radiative transfer calculations on the whole observable disk at every interval of 4^o of latitude and longitude.

N_2 and CO_2 gases are assumed to be well-mixed for with abundances corresponding

to the table 2.0.2.

H_2O and C_{LW} are ingested from ExoPlaSim model. We assume that those quantities have horizontally and vertically inhomogeneous distributions. H_2O and C_{LW} are crucial for planetary habitability and their abundances propagate into the simulated spectra. For the spectral simulations, the size of liquid water particles in clouds is required. Note that ExoPlaSim does not compute liquid water particle size in clouds, nor ice water content and particle size due to model simplifications. Because of this, we adopt a global value of 0.5 μm for liquid water particle size in clouds, based on previous studies (Igel and van den Heever, 2017a,b). This is a common issue in characterizing the climate of Earth-like planets, as clouds are notoriously difficult to represent correctly in GCMs due to their characteristic timescales and sizes (Fauchez et al., 2022). Additionally, even for Earth climate models, it is challenging to characterize clouds and aerosols (Wunderlich, Fabian et al., 2019). This is why we compute the spectra for two different cases: (a) considering water clouds and (b) without water clouds.

Molecular absorptions for N_2, CO_2, and H_2O are incorporated using correlated-k tables derived from the HITRAN 2020 database (Gordon et al., 2022). Aerosol properties are modeled using Mie Scattering theory, with water cloud scattering properties as described in Massie and Hervig (2013). Ice cloud optical properties are not included as these are not considered by ExoPlaSim. For this we defined the number of n-stream pairs equal to 4 and the number of scattering Legendre polynomials used for describing the phase function equal to 60. This is defined the same for both spectra cases.

Rayleigh scattering is considered, with cross sections calculated as a sum of the individual molecular cross sections, which are wavelength-dependent based on molecular polarizability.

Collision-induced absorptions (CIAs) arising from inelastic molecular collisions in a gas are included using HITRAN CIA compilations (Gordon et al., 2022) and the HITRAN CIA database (Karman et al., 2019). In the spectral range considered, the significant CIAs are those of CO_2˘CO_2, N_2˘H_2O, and N_2˘N_2. PSG integrates the MT_CKD water continuum (Mlawer et al., 2012) by transforming it to CIAs of H_2O˘H_2O (Kofman and Villanueva, 2021). t We implement a geometric observation model for an emission disk with direct imaging to obtain

both emission and reflection spectra of the planets. This allows us to investigate the characteristics of the planet's thermal emission as well as its optical regime, where we can infer the existence of clouds through the reflection spectra (Hedelt et al., 2013). As Hedelt et al. (2013) states, "the emergent spectrum holds information about the temperature structure of the atmosphere as well as the atmospheric components". For direct imaging, radiative transfer simulations are conducted across the entire observable disk, and the individual spectra are integrated based on the projected area of each bin (Villanueva et al., 2018).

We assume that the planet is observed from Earth at a distance of 1 Pc, with the planet 1 AU from its host star. We obtained the spectra for the quadrature geometry case (phase of 90^o), where the planet is half illuminated. We selected this phase because, according to Krissansen-Totton et al. (2016), the probability distribution of the apparent phase for a direct imaging observation of an exoplanet with a random inclination and position in its orbit suggests that it is more likely to find the exoplanet in quadrature phase.

Remembering that the scope of this work is to examine the observable changes in the spectra due to variations in atmospheric parameters related to changes in obliquity, rather than instrument-specific detection capabilities, we simulate spectra using an instrument reminiscent of the JWST/MIRI instrument, with some modifications for our analysis. We extend the spectral range to 0.3 to 30 μm and set a resolving power (R) of 100. We choose this spectral band because thermal emission from the planet and its spectral signatures of water are more relevant in IR and Mid-IR. Signal-to-noise ratios are not considered.

Chapter 3

Results

The objective of this section is to present the results of the General Circulation Model (GCM) and Radiative Transfer (RT) model simulations based on the Archean-Earth-like aquaplanet model. This section is divided into two parts: the atmospheric simulation of the aquaplanets and the emission and reflection spectra simulations derived from the GCM data.

3.0.1 Atmospheric Simulation

First, we analyzed the net radiative flux at TOA to verify whether the climate of the aquaplanets are in equilibrium. For all 10 aquaplanet simulations, the net radiative flux at TOA values are near zero, indicating that the climate of aquaplanets have reached the equilibrium. All simulations reached it approximately by the 80th year from the start of the simulation (not shown).

Figure 3.0.1 represents the habitability over the annual cycle, both zonally and globally. To calculate percentage of surface habitability throughout the year first, we computed the Wet Bulb Temperature (T_W) for all latitudes, longitudes, and atmospheric level closest to the surface. Then, we calculate the long-term mean (lastest 50 years) of T_W for each month. This means that we average T_W over the 50 years for each month separately. We then selected one month of the year, averaging T_W longitudinally. Next, we identified latitudinal points that met the habitability condition of T_W in one month. Latitudes meeting this condition were assigned a score of 1, and those that did not were assigned a score of 0. This process was repeated for each of the 12 months of the year and for each of

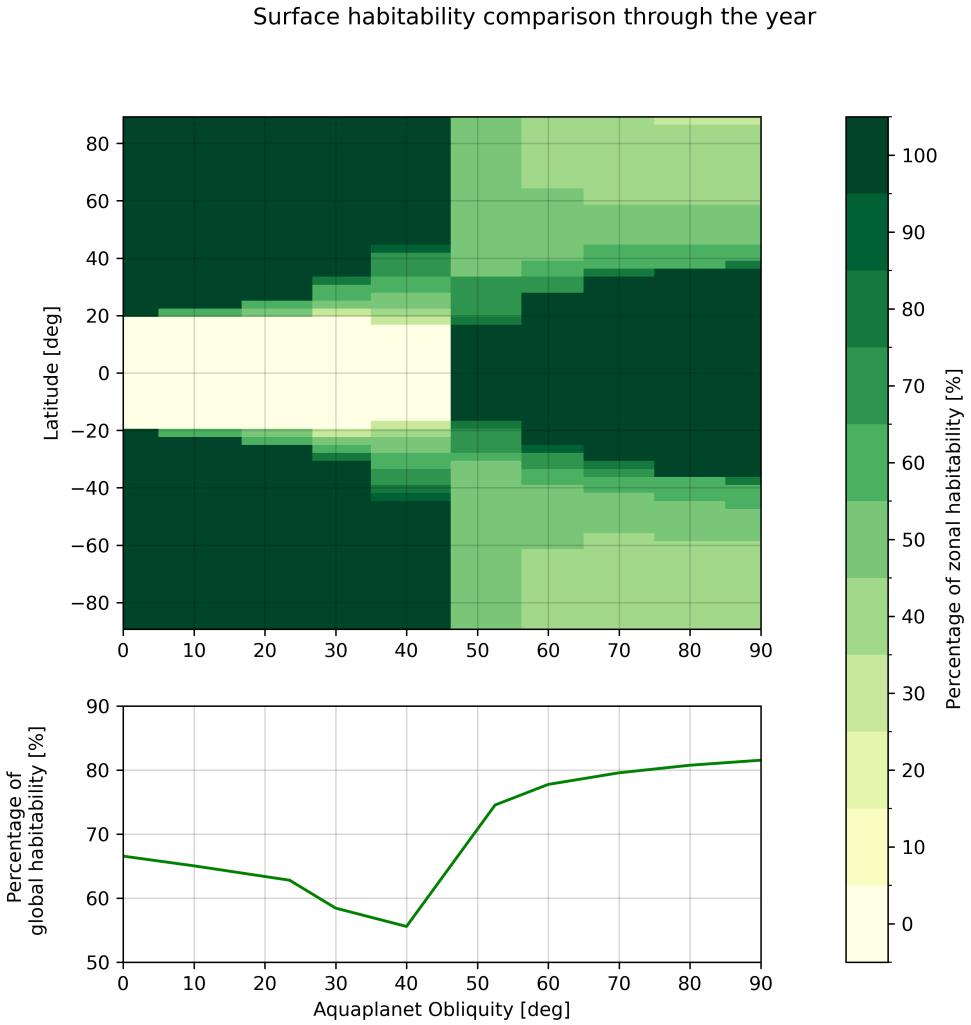

Figure 3.0.1: Percentage of surface habitability throughout the year comparison for 10 aquaplanet simulations. This shows the latitudes that fulfill the condition of Wet Bulb Temperature (T_W) between 273.15 and 308.15 K. The upper panel shows the latitudinal distribution of surface habitability for each simulation. The bottom panel shows the global average of surface habitability for each simulation.

the 10 simulations. Thus, each latitude and simulation had a habitability score ranging from 0 to 12, which we converted to the percentage of the year meeting the habitability condition (see upper panel of Figure 3.0.1). For global habitability, we averaged the latitudinal scores for each simulation, applying a cosine weighting for latitude due to the larger surface area near the equator compared to the poles.

The upper panel of Figure 3.0.1 shows that for latitudes between -20^o and 20^o are uninhabitable year-round for $\phi = 0^o$, while latitudes from $\pm 20^o$ to the poles are habitable 100% the year. Simulations with ϕ between 0^o and 40^o show that the year-round habitable regions shrink, and the uninhabitable regions expand to latitudes near $\pm 30^o$ as obliquity increases. A notable case is $\phi = 40^o$, where the year-round uninhabitable region shrinks to latitudes between $\pm 17^o$, but the uninhabitable region extends to latitudes $\pm 45^o$ in both hemispheres. Between $\phi = 40^o$ and $\phi = 52.5^o$, there is a regime shift where the surface between latitudes $\pm 17^o$ becomes habitable year-round, and areas between $\pm 17^o$ and the poles are habitable only part of the year. As obliquity increases, year-round habitable regions expand, while regions closer to the poles decrease in annual habitability percentage. At $\phi = 90^o$, the year-round habitable region reaches latitudes near $\pm 36.5^o$.

The lower panel of Figure 3.0.1 shows the global habitability percentage over the year. For $\phi = 0^o$, it is 66.5%, decreasing with increasing obliquity to a minimum of approximately 55.6% at $\phi = 40^o$. Between $\phi = 40^o$ and $\phi = 52.5^o$, there is a regime change where global habitability increases, reaching 74.6% at $\phi = 52.5^o$ and a maximum of 81.5% at $\phi = 90^o$.

Figure 3.0.2 shows the zonally averaged Wet Bulb Temperature (T_W) for the atmospheric layer closest to the surface. The figure presents three temporal averages: annual (upper panel), DJF (middle panel), and JJA (bottom panel).

The annual mean surface T_W for $\phi = 0^o$ shows habitable ranges at latitudes between 20^o and 90^o for each hemisphere. This pattern repeats do not change throughout the year. For the Earth analog ($\phi = 23.5^o$), the habitable and uninhabitable regions based on T_W are similar to those of $\phi = 0^o$. The main difference is that the T_W temperature outside the tropics increases, so the meridional T_W gradient decreases.

For $\phi = 40^o$, the annual mean T_W indicates habitable ranges at latitudes greater

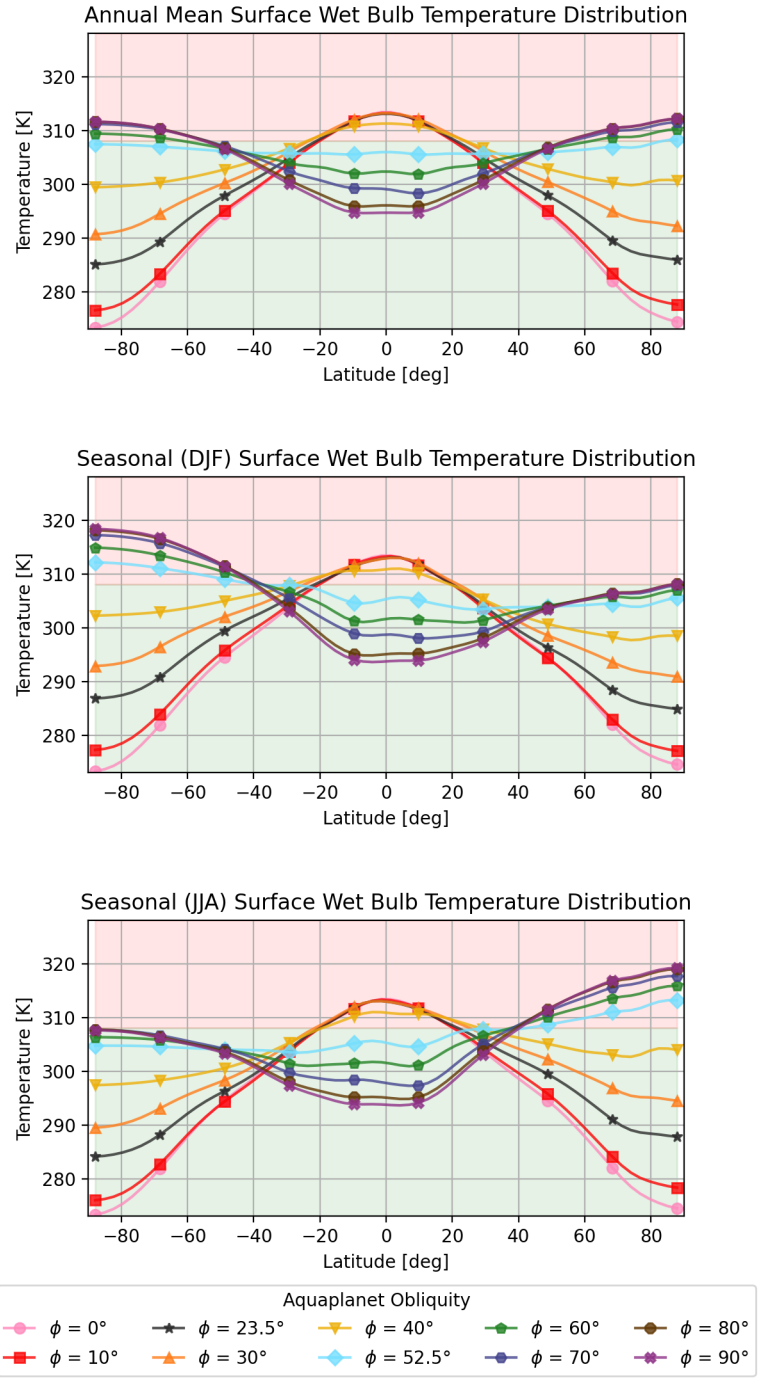

Figure 3.0.2: Latitudinal distribution of Zonal Surface Wet Bulb Temperature for 10 different simulations with varying obliquity: **Upper panel**: Annual Mean, **Middle panel**: DJF Seasonal Mean, and **Bottom panel**: JJA Seasonal Mean. Each aquaplanet is represented by a characteristic color and marker. The green/red filled backgrounds represent the habitable/inhabitable ranges for T_W.

than 25^o up to 90^o of each hemisphere. For DJF, the habitable region shifts to latitudes greater than 20^o and less than -30^o, while in JJA, the opposite pattern is observed. From this obliquity the seasonal variability in the T_W is more evident and thus the habitability too.

A transition in T_W behavior is seen between $\phi = 23.5^o$ and $\phi = 52.5^o$. At $\phi = 52.5^o$, the annual mean T_W suggests that the entire planet is habitable. However, seasonal means show that latitudes between -40^o and -90^o are uninhabitable in DJF and latitutes between 40^o and 90^o are uninhabitable in JJA. This case shows the smallest temperature difference between the equator and poles compared to other obliquities, aligning with Nowajewski et al. (2018), who noted that this obliquity results in zero equator-to-pole difference of incoming solar radiation at the TOA (see figure 4.1 from Nowajewski et al. (2018)).

For $\phi = 90°$, the annual mean T_W shows habitable latitudes between 55° and $-55°$, with uninhabitable regions beyond these latitudes. Unlike the aquaplanets with $\phi = 52.5^o$, the seasonal T_W distribution of $\phi = 90°$ reveals inverted temperature meridional gradients compared to lower obliquities. $\phi = 90°$ shows uninhabitable conditions at latitudes less than $-40°$ in DJF and greater than 40° in JJA.

The annual and seasonal mean T_W for $\phi = 0°$ shows the largest temperature gradient between the equator and poles, about 40 K for both cases, which decreases with increasing obliquity, becoming nearly zero at $\phi = 52.5°$. Beyond this, the gradient inverts, with poles reaching higher temperatures than the tropics at higher obliquities.

Figure 3.0.3 shows the zonally averaged Sea Surface Temperature (T_S), similar to Figure 3.0.2, but focusing only on the annual mean due to similar seasonal behavior observed in T_S and T_W.

All simulations show T_S above the freezing point of water, given the atmospheric pressure of 1000 hPa, indicating no surface ice and satisfying our habitability criterion. Maximum surface temperatures reach approximately 320 K across simulations, varying latitudinally with obliquity. At 0^o obliquity, the maximum temperatures are between latitudes -25^o and 25^o, while at 90^o obliquity, they are near the poles.

The annual mean T_S and T_W show similar patterns across all aquaplanets. The same seasonal behavior observed in T_W is reflected in T_S for all simulations.

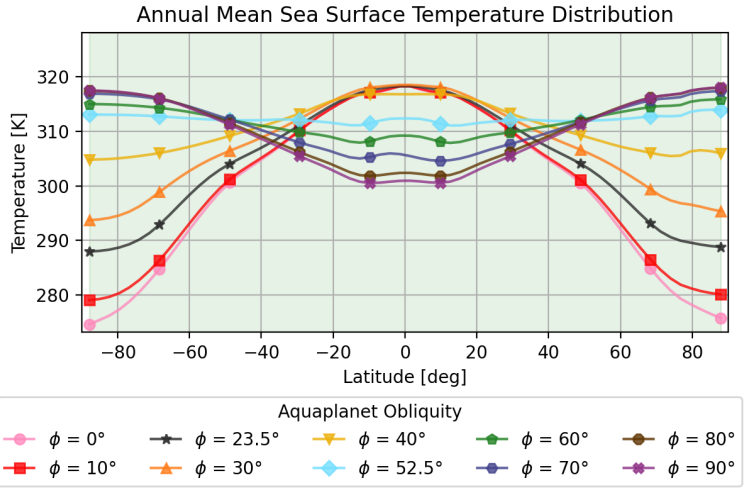

Figure 3.0.3: Latitudinal distribution of the Annual Mean of Zonal Surface Sea Temperature for 8 different simulations with varying obliquity. Each aquaplanet is represented by a characteristic color and marker. The green filled background represents the habitable ranges for T_S.

Figure 3.0.4 presents the variables obtained from ExoPlaSim: air temperature, specific humidity, and liquid water content in clouds. These variables are crucial for understanding the spectral behavior of each aquaplanet and are input into the PSG model. Morever, air temperature and humidity are the variables to constrain habitability at surface level.

For Figure 3.0.4, we plotted air temperature, specific humidity, and liquid water content in clouds, averaged annually and zonally for all atmospheric layers. We selected four cases of interest for comparison: $\phi = 0^o$ and $\phi = 90^o$ as extreme obliquities, and $\phi = 40^o$ and $\phi = 52.5^o$ due to the observed regime shift in habitability between these obliquities (see Figure 3.0.1). The $\phi = 40^o$ case shows the lowest annual surface habitability, while $\phi = 52.5^o$ exhibits minimal annual latitudinal temperature gradient and the smallest equator-to-pole temperature difference compared to other simulations. Although $\phi = 23.5^o$ represents modern Earth's obliquity, its behavior is very similar to $\phi = 0^o$, so we omitted it for comparison.

For $\phi = 0^o$, the annual mean of air temperature (T_A) is around 300 K at the surface between latitudes $-50°$ and 50^o, decreasing towards the poles to about 270 K. Independent of latitude, T_A decreases with altitude, but vertical gradient of T_A is different for each latitude, being greater at the poles than at the equator. This

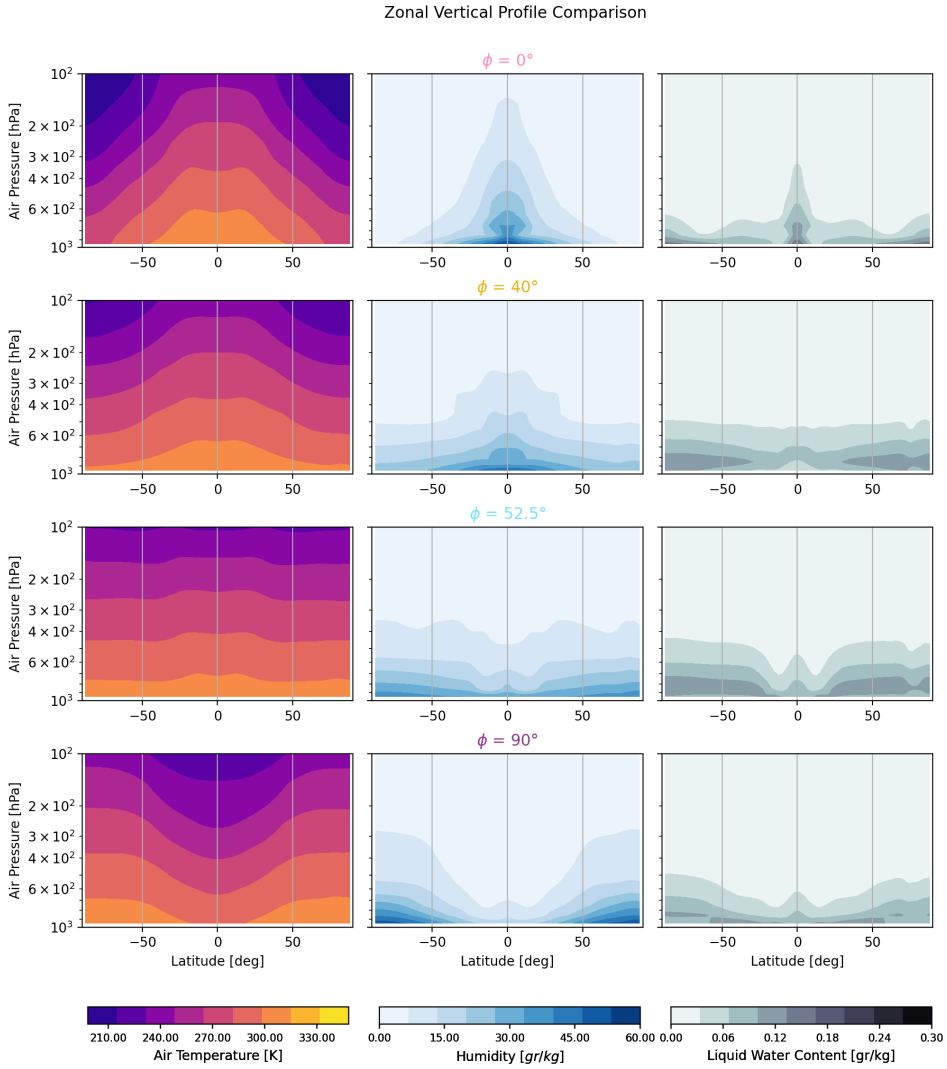

Figure 3.0.4: Comparison of annual zonal vertical profiles of **(a)** Air temperature, **(b)** Specific humidity, and **(c)** Liquid water content in clouds of Archean Earth-like aquaplanets. Each row represents the selected cases of $\phi = 0°, 40°, 52.5°, 90°$ with their respective colors. Notable differences in water content between gaseous and liquid phases are observed between the simulations.

is probably due to the distribution of water vapor in the atmosphere, being greater at low latitudes than at high latitudes. If the air becomes saturated with water vapor, it releases latent heat as it condenses and dampens temperature changes with altitude (chapter 3 Wallace and Hobbs (2006)). The highest concentrations of water vapor are found between 20^o and the equator. The liquid water content of clouds is also highest at the equator.

For $\phi = 40^o$, the latitudinal gradient of near-surface T_A is smaller compared to $\phi = 0^o$. At higher altitudes, at high latitudes this feature is maintained, but the latitudinal gradient of T_A is still smaller than for $\phi = 0^o$. Specific humidity follows a similar pattern, with higher values at the equator, decreasing towards the poles, and a smaller gradient than $\phi = 0^o$. Liquid water content in clouds shows a distinct pattern: between 900 hPa and the surface, water content increases from the equator to the poles. Vertically, water content increases up to 700 hPa between latitudes -30^o and 30^o, then decreases above this pressure. A similar pattern is observed between latitudes $\pm 30^o$ and $\pm 60^o$. At latitudes 80^o, liquid water content decreases between 1000 hPa and 900 hPa.

For $\phi = 52.5^o$, the near-surface T_A shows almost no equator-to-pole gradient. At 700 hPa, T_A is highest near $\pm 15^o$, decreasing towards the poles and equator. At altitudes below 700 hPa, the highest temperatures are near the equator, decreasing slightly towards the poles. The temperature gradient for $\phi = 52.5^o$ is much smaller compared to other simulations. Specific humidity is highest at the poles near the surface, with a smaller gradient than other simulations. At 850 hPa, the highest specific humidity is at the poles, decreasing to $\pm 13^o$, then increasing towards the equator. A similar pattern is observed up to 665 hPa, above which the gradient is only from equator to poles. Liquid water content in clouds for $\phi = 52.5^o$ shows a similar pattern to specific humidity, with a positive equator-to-pole gradient between 910 hPa and 880 hPa, and a negative gradient from the equator to $\pm 10^o$, becoming positive from $\pm 10^o$ to the poles. At 80^o latitude, there is a decrease in liquid water content between 1000 hPa and 860 hPa, which reappears between 830 hPa and 720 hPa.

For $\phi = 90^o$, the patterns are similar to $\phi = 0^o$ but with inverted gradients. Annual T_A is lowest at the equator, increasing towards the poles. Specific humidity is highest at the poles, decreasing towards the equator, with different behavior between 915 hPa and 700 hPa, where the gradient is negative from the equator

to $\pm 10^o$, then positive from $\pm 10^o$ to the poles. For pressures below 700 hPa, the gradient is positive, similar to the surface. Liquid water content in clouds for $\phi = 90^o$ shows a positive gradient from the equator to $\pm 55^o$ between 1000 hPa and 875 hPa, then negative from $\pm 55^o$ to the poles. Between 875 hPa and 810 hPa, there is higher cloud water content, with greater latitudinal extent in the southern hemisphere. For pressures below 810 hPa, a negative equator-to-pole gradient is observed from the equator to $\pm 13.5^o$, then positive from $\pm 13.5^o$ to the poles. From Figure 3.0.4 we can note that for each of the 4 cases of interest, there is a particular distribution for the specific humidity and the cloud liquid water content.

3.0.2 Spectral Simulation

We computed the radiance spectra for all 10 aquaplanet simulations. To calculate the radiance spectra (emission and reflection), we used the annual average of the last 50 years of variables calculated by ExoPlaSim. We simulated two different cases: including and excluding clouds. For the cloudless case, we simply excluded the cloud liquid water content variable from the spectral calculations.

Our analysis focuses on water vapor (H_2O), liquid water clouds, and CO_2 because of their relevance to habitability (Hedelt et al., 2013; Suissa et al., 2020). H_2O is related to specific humidity, while CO_2 is strongly linked to air temperature (T_A) response (Hedelt et al., 2013). Both humidity and T_A are used to determine the Wet Bulb Temperature (T_W), our habitability indicator. Clouds, represented by the water content in clouds (C_{LW}) computed by ExoPlaSim, significantly impact a planet's spectral appearance (Fauchez et al., 2019; Hedelt et al., 2013).

From the top panel of Figure 3.0.5, we observe the emission and reflection spectra of the aquaplanets, excluding clouds. The bottom panel shows the emission and reflection spectra of the same cases including the observational effect of clouds. In the cloudless case, at wavelengths shorter than 0.7 μm, corresponding to the UV and visible bands, we see the reflection of the host star's spectrum. The drop in reflected light from the UV to Near-IR follows the drop of the stellar light blackbody curve on that band. In the mid-IR, we can see the emission spectra of the aquaplanets. Stellar spectrum reflection can be seen at wavelengths up to 4 μm (Hedelt et al., 2013). But the planet's emission spectrum is dominant at wavelengths longer than 2.7 μm.

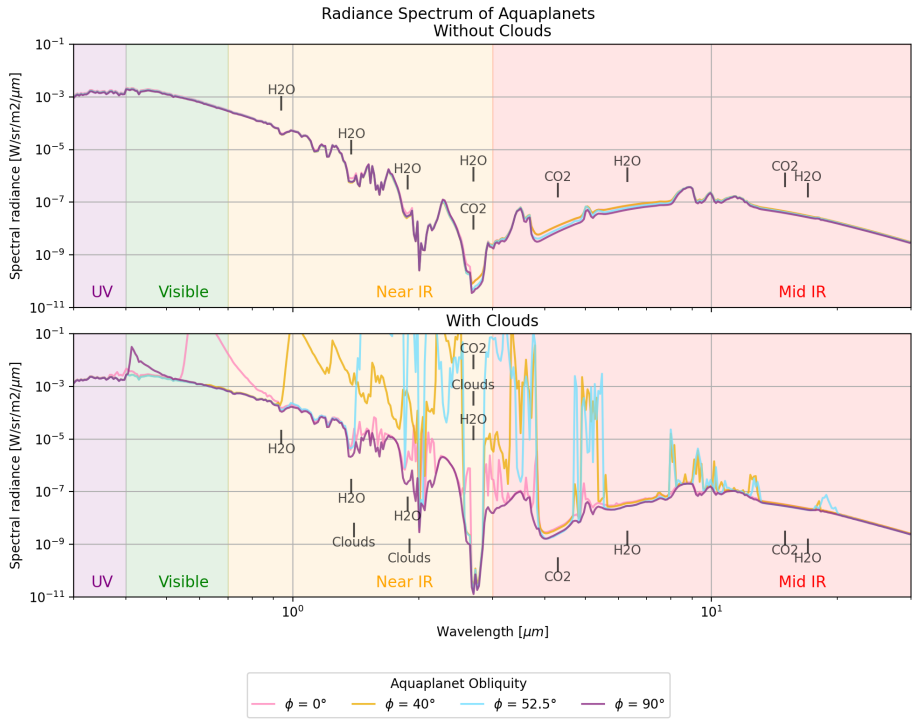

Figure 3.0.5: Radiation spectrum of the selected aquaplanets. The **upper panel** shows the spectrum without the observational effect of clouds. The **bottom panel** includes the observational effect of clouds. The purple/green/orange/orange/red colored background represents the UV/Visible/NIR/MidIR bands of the electromagnetic spectrum. Labeled are the absorption lines of H_2O, CO_2 and Clouds. The spectrum shows both reflected and emitted light from aquaplanets.

When clouds are included (bottom panel of Figure 3.0.5), super emissions of radiation (hereafter referred to as "flares") are distributed differently depending on the planet's obliquity. These flares are presumably caused by calculation errors in PSG due to the inclusion of clouds. As noted by Fauchez et al. (2022), it is challenging to accurately include clouds in both GCM and RT simulations. Consequently, reliable results for the emission spectra of aquaplanets including clouds are unattainable. Correcting this effect will be addressed in future work. Therefore, we focus on analyzing the spectral components of the cloudless simulations.

In the cloudless case, absorption lines of H_2O are observed at 0.94, 1.4, 1.9,2.7, 6.3 μm (see Figure 3.0.6). These absorption lines are due to water vapor and are consistent with previous studies (Ding and Wordsworth, 2022; Fauchez et al., 2022; Hedelt et al., 2013; Smith et al., 2020; Suissa et al., 2020; Wunderlich, Fabian et al., 2019). In Figure 3.0.6 we can see notable spectral responses to changes in obliquity. They are seen at 2.7 μm in the near-IR and at 6.3 μm in the mid-IR. In both cases, the $\phi = 90^o$ simulation shows strong absorption, while $\phi = 40^o$ has weaker absorption due to water vapor. The 2.7 μm absorption line overlaps with CO_2 absorption. The same pattern is observed in the 17.0 μm band. Although the, and 17.0 μm is overlaped with CIAs absorption band. For the 0.94 μm absorption line, this characteristic difference in absorption depth between $\phi = 40^o$ and $\phi = 90^o$ is not observed. For the 1.4 and 1.9 μm lines, there are differences in absorption depth, but they do not have the same characteristics as the water vapor response at 2.7 and 6.3 μm. When clouds are included, the only distinguishable spectral response of H_2O is at 2.7 μm, where intense absorption due to clouds is noted. The presence of clouds obscures information about water vapor, making the characteristic difference between $\phi = 40^o$ and $\phi = 90^o$ barely noticeable at this wavelength.

For the cloudless case, CO_2 absorption is observed near 2.7, 4.3, and in the 15.0 μm band, consistent with (Fauchez et al., 2022; Hedelt et al., 2013). Also in 9.5, and 10.5 μm we can observe weak absorption of CO_2 which is consistent with Salamah et al. (2022) radiation absorption percentage of CO_2 found in the Earth's atmosphere. In the 4.3 μm band, the same spectral response to obliquity changes observed in the H_2O and CO_2 absorption at 2.7 μm is repeated. This behavior is also observed in the 6.3 μm band shared with H_2O, though much weaker. In

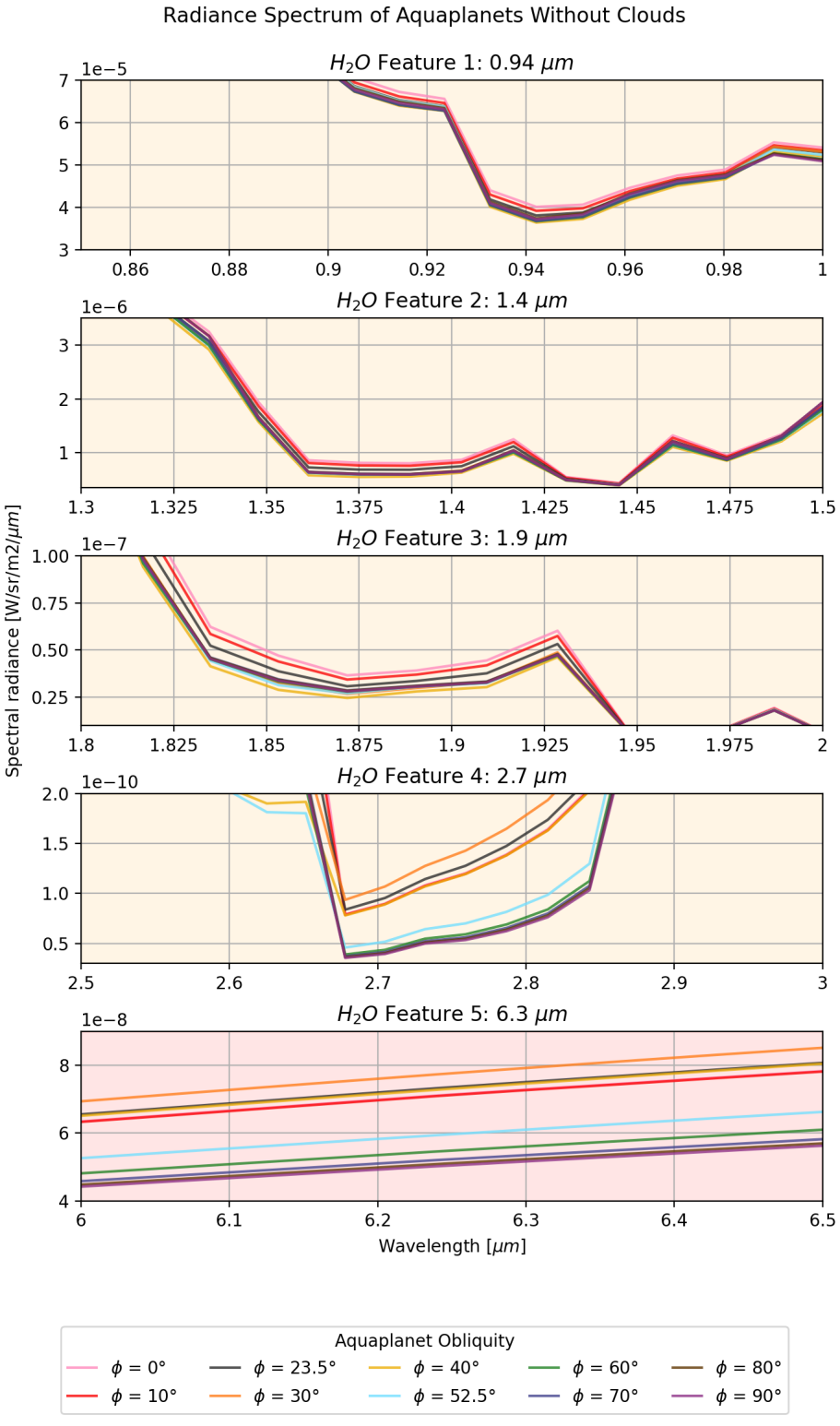

Figure 3.0.6: Spectral features of H_2O of all aquaplanets without incluiding clouds. 0.94, 1.4, 1.9, 2.7, 6.3 μm spectral features are represented in each row. The coloured filled background represents the spectral bands that correspond each panel. Orange color represents the Near-IR and red represents Mid-IR.

the spectral simulation with clouds, the only observable feature caused by CO_2 is the 2.7 μm line. The presence of clouds almost completely blocks the spectral response of CO_2 to air temperature.

In the cloudless case, absorption caused by collision-induced absorptions (CIAs) of the $CO_2 - CO_2$ pair is observed in the 3.0 to 4.0 μm band. The spectral response of $N_2 - H_2O$ and $N_2 - N_2$ in the 3.5-5.1 μm band is obscured by the CO_2 absorption band at 4.3 μm. Absorption due to $N_2 - N_2$ CIAs is observed at 2.1 μm. We also observe absorption starting from 13.0 to 30.0 μm caused by the $CO_2 - CO_2$, $H_2O - H_2O$, and $N_2 - N_2$ colissional pairs. This absorption obscures the spectral features of CO_2 and H_2O in that band. When clouds are included, reliable information of CIAs cannot be derived due to the significant impact of clouds on the spectra.

Chapter 4

Discussion

4.0.1 Summary of Key Findings

Our study confirms the previously observed climate effects dependent on obliquity as reported by Nowajewski et al. (2018). Specifically, we observed a direct relationship between obliquity and the latitudinal and atmospheric level distribution of air temperature, humidity, and cloud coverage. Additionally, the climatic regime shift noted in aquaplanets with obliquities below and above 52.5° is also replicated in our findings. The aquaplanet with an obliquity of 90° was found to be the most globally habitable throughout the year, while the one with an obliquity of 40° was the least. However, in the case of $\phi = 90°$, one of the poles becomes uninhabitable depending on the season (i.e., DJF or JJA). In contrast, the aquaplanet with $\phi = 0°$ maintains consistent habitable and uninhabitable regions throughout the year. We encountered significant challenges in accurately modeling the impact of clouds on the radiance spectra of the aquaplanets. Consequently, our spectral analysis predominantly focuses on cloudless aquaplanets. This limitation is consistent with the inherent difficulty in representing clouds correctly in GCMs due to their small-scale processes and complex physical interactions (Fauchez et al., 2022). In general, the radiance spectra of the aquaplanets are nearly identical regardless of changes in obliquity. However, variations were observed in spectral lines and bands associated with H_2O and CO_2. Notable differences were detected in the water vapor spectral features at 2.7 and 6.0 μm, indicating some degree of spectral variation between aquaplanets with different obliquities.

4.0.2 Interpretation of Results

Due to the fact that H_2O is related to humidity (q) and CO_2 is strongly linked to air temperature (T_A) (Hedelt et al., 2013), and both q and T_A are related to Wet Bulb Temperature (T_W), our habitability indicator, we can infer that the observed effect in the 2.7 and 6.0 μm water vapor absorption lines in the cloudless case might be connected to the global habitability percentage throughout the year, as shown in Figure 3.0.6. From the bottom panel of Figure 3.0.1 and Figure 3.0.6, we could infer a relationship between habitability and the 2.7 μm absorption line. For example, in the case of $\phi = 90^o$, higher absorption correlates with higher observed habitability. This correlation aligns with the orbital effects of obliquity. For $\phi = 90^o$, solar irradiance alternates between poles throughout the year, increasing the habitable area compared to $\phi = 40^o$. On the other hand, for $\phi = 40^o$, despite having similar air temperature and humidity to $\phi = 52.5^o$, Figure 3.0.1 shows it is less globally habitable due to obliquity effects. The more direct equatorial solar irradiance at $\phi = 40^o$ leads to greater uninhabitability in that region. This covers a larger surface area compared to $\phi = 52.5^o$, a distinction visible in the emission spectrum. This effect is apparent only when cloud effects are ignored, as clouds overlap the humidity impact at 2.7 μm (see bottom panel from Figure 3.0.5). However, we must be careful with this assumption because clouds in this work are not well parametrized. Including the other cases excluded from the spectral analysis of Figure 3.0.5, it becomes apparent that the correlation between habitability and absorption at 2.7μm is not straightforward (see Figure 3.0.6). For instance, $\phi = 0^o$ and $\phi = 40^o$ show nearly equal absorption. However, when considering all cases, we can note 2 different regimes. The first regime consists of less habitable Earth-Archean type planets with lower absorption at the 2.7μm line, including obliquities $\phi = 0^o, 10^o, 23.5^o, 30^o, 40^o$. The second regime comprises more habitable Earth-Archean type planets with higher absorption at the 2.7μm line, including obliquities $\phi = 52.5^o, 60^o, 70^o, 80^o, 90^o$. In this second regime, we may presume a correlation between absorption at that line and habitability, which is not observed in the first regime.

4.0.3 Implications

If this method were to be tested with other GCM and RT models and the relationship between obliquity and spectral behavior confirmed, it could provide

a new approach for interpreting the orbital information of exoplanets based on spectroscopic observations. Establishing a consistent link between habitability, as measured by T_W, and spectral response would suggest that this model could offer a way to observe habitability. Distinguishing habitability and obliquity through spectral features might be applicable primarily to cases with obliquities of 52.5° or higher. However, this potential application is contingent on having the necessary observational capabilities to measure these spectral features accurately. Only with advanced observational technology could the spectral analysis be leveraged to infer exoplanetary habitability and orbital characteristics reliably. Despite this, our method provides valuable insights that could inform the development of future telescope projects and observational strategies.

4.0.4 Limitations

The limitations of this works are related to the General Circulation Model (GCM) used and the simplifications inherent in the model, which omit important microphysical processes. Additionally, we used only one GCM, so we lack validation against other models to confirm our results. The effect of our cloud modeling on the spectrum and the necessary instrumentation to compare results accurately also pose significant challenges. We are uncertain about the detectability of the 2.7 and 6.0 μm features, as we do not have reliable spectral results considering clouds. Even though we excluded clouds in the analysis of these lines, clouds are inherently present and can influence the results. Furthermore, we did not conduct an observability measurement to understand how detectable these features would be in actual observations, considering signal-to-noise ratios (S/N) and other observational effects.

4.0.5 Future Work

Future studies should focus on simulating the detectability of these signals while considering noise and instrumentation effects will be crucial for determining the practical observational capabilities required to detect these spectral features. Moreover, improving the GCM to include microphysical processes is crutial to enable the calculation of both water and ice clouds along with the size of water and ice particles. Enhancing the model to include the effects of other significant greenhouse gases, such as CH_4. Improving the archaic model to incorporate an

Archean-Sun would also be beneficial. Additionally, it is crucial to broaden the definition of habitability with T_W to include species other than mammals. For example, investigating data on archaea that live in the air and have a preferred T_W could provide new insights. Improving the spectroscopic modeling of clouds and analyzing the 2.7 and 6.0 μm lines to determine if there is a link between absorption and habitability for $\phi = 52.5^o, 60^o, 70^o, 80^o, 90^o$ is essential. According to Hedelt et al. (2013) and Fauchez et al. (2019), clouds can significantly impact the spectral appearance of a planet. Finally, understanding whether there is a correlation between the absorption features in the emission spectra of aquaplanets at the 2.7 and 6.0 μm lines and T_W remains a critical area of investigation.

Chapter 5

Conclusion

In this work, we investigated the interplay among planetary obliquity, atmospheric thermodynamics, and hydrological processes and their impact on the habitability and spectroscopic properties of aquaplanets with an Archean Earth-like atmospheric composition. Our study confirms that the obliquity of an Archean-Earth-like aquaplanet influences its atmospheric thermodynamics, surface habitability, and observables like the emission spectrum. We corroborate the findings of Nowajewski et al. (2018) that there is a characteristic atmospheric behavior in aquaplanets dependent on obliquity, even when the atmospheric CO_2 concentration is altered to match that of the Archean Earth. Notable cases include obliquities of 0^o, 40^o, 52.5^o, and 90^o, each showing distinct patterns in air temperature, humidity, liquid water in clouds, and habitability.

On the radiative aspect, we were unable to accurately model the spectral behavior of clouds, consistent with the challenges noted by Fauchez et al. (2022). The radiance spectra of the aquaplanets are nearly identical across different obliquities. However, for cloudless planets, spectral features related to H_2O and CO_2 show variations that seem connected to obliquity. The 2.7 and 6.0 μm water vapor features, in particular, appear to correlate with our habitability parameter T_W for obliquities greater than or equal to 52.5^o. This spectral behavior linked to T_W is not observed for aquaplanets with obliquities less than or equal to 40^o.

This study gives light on the potential characteristics and observable features of an Archean-like atmosphere. It proposes a simple model that varies only one orbital parameter to understand its effect on climate and observability of exoplanets.

Our findings provide insights into which parts of the spectrum might indicate habitability and could inform future telescope missions on which spectral bands to focus on for observing these characteristics.

To improve our model, it is crucial to include microphysical processes in the GCM, affecting habitability and the calculation of important variables for cloud modeling. Additionally, considering the radiative effect of significant greenhouse gases like CH_4 is essential. Properly modeling the observational impact of clouds remains a critical area for improvement. It is necessary to confirm with other GCM and RT models whether the spectral features observed at 2.7 and 6.0 μm are indeed linked to T_W.

Moreover, analyzing the detectability of the 2.7 and 6.0 μm spectral features with existing or future telescopes, considering noise and other attenuating effects, is crucial. This could be particularly useful for future telescopes like LUVOIR, HabEx (Komacek and Abbot, 2019), and MERECLE (Mandell et al., 2022). If the obliquity-climate-spectrum relationship is confirmed, this method could help determine or validate obliquity estimates of water-covered exoplanets based on spectroscopic observations.

Future research should delve into the atmospheric dynamics of the Archean-like atmosphere and its link to obliquity under the proposed model. It is also important to analyze whether the effects of obliquity on atmospheric dynamics, habitability, and spectra persist when including continents, changing the orbital period, altering the host star type, or considering the host star's age.

Bibliography

Arney, G., Domagal-Goldman, S. D., Meadows, V. S., Wolf, E. T., Schwieterman, E., Charnay, B., Claire, M., Hébrard, E., and Trainer, M. G. (2016). The pale orange dot: The spectrum and habitability of hazy archean earth. *Astrobiology*, 16(11):873–899. PMID: 27792417.

Bahcall, J. N., Pinsonneault, M. H., and Basu, S. (2001). Solar models: Current epoch and time dependences, neutrinos, and helioseismological properties. *Astrophys. J.*, 555:990–1012.

Carr, M. H. and Head, J. W. (2010). Geologic history of mars. *Earth and Planetary Science Letters*, 294(3):185–203. Mars Express after 6 Years in Orbit: Mars Geology from Three-Dimensional Mapping by the High Resolution Stereo Camera (HRSC) Experiment.

Catling, D. C. and Zahnle, K. J. (2020). The archean atmosphere. *Science Advances*, 6(9):eaax1420.

Chen, H., Li, G., Paradise, A., and Kopparapu, R. K. (2023). Sporadic spin-orbit variations in compact multiplanet systems and their influence on exoplanet climate. *The Astrophysical Journal Letters*, 946(2):L32.

Childs, A. C., Martin, R. G., and Livio, M. (2022). Life on exoplanets in the habitable zone of m dwarfs? *The Astrophysical Journal Letters*, 937(2):L41.

Ding, F. and Wordsworth, R. D. (2022). Prospects for water vapor detection in the atmospheres of temperate and arid rocky exoplanets around m-dwarf stars. *The Astrophysical Journal Letters*, 925(1):L8.

do Nascimento Vieira, A., Kleinermanns, K., Martin, W. F., and Preiner, M. (2020). The ambivalent role of water at the origins of life. *FEBS Letters*, 594(17):2717–2733.

Donohoe, A. and Battisti, D. S. (2011). Atmospheric and surface contributions to planetary albedo. *Journal of Climate*, 24(16):4402 – 4418.

Fauchez, T. J., Turbet, M., Villanueva, G. L., Wolf, E. T., Arney, G., Kopparapu, R. K., Lincowski, A., Mandell, A., de Wit, J., Pidhorodetska, D., Domagal-Goldman, S. D., and Stevenson, K. B. (2019). Impact of clouds and hazes on the simulated iJWST/i transmission spectra of habitable zone planets in the TRAPPIST-1 system. *The Astrophysical Journal*, 887(2):194.

Fauchez, T. J., Villanueva, G. L., Sergeev, D. E., Turbet, M., Boutle, I. A., Tsigaridis, K., Way, M. J., Wolf, E. T., Domagal-Goldman, S. D., Forget, F., Haqq-Misra, J., Kopparapu, R. K., Manners, J., and Mayne, N. J. (2022). The trappist-1 habitable atmosphere intercomparison (thai). iii. simulated observables—the return of the spectrum. *The Planetary Science Journal*, 3(9):213.

Fraedrich, K., Jansen, H., Kirk, E., Luksch, U., and Lunkeit, F. (2005). The planet simulator: Towards a user friendly model. *Meteorologische Zeitschrift*, 14(3):299–304.

Gordon, I., Rothman, L., Hargreaves, R., Hashemi, R., Karlovets, E., Skinner, F., Conway, E., Hill, C., Kochanov, R., Tan, Y., Wcisło, P., Finenko, A., Nelson, K., Bernath, P., Birk, M., Boudon, V., Campargue, A., Chance, K., Coustenis, A., Drouin, B., Flaud, J., Gamache, R., Hodges, J., Jacquemart, D., Mlawer, E., Nikitin, A., Perevalov, V., Rotger, M., Tennyson, J., Toon, G., Tran, H., Tyuterev, V., Adkins, E., Baker, A., Barbe, A., Canè, E., Császár, A., Dudaryonok, A., Egorov, O., Fleisher, A., Fleurbaey, H., Foltynowicz, A., Furtenbacher, T., Harrison, J., Hartmann, J., Horneman, V., Huang, X., Karman, T., Karns, J., Kassi, S., Kleiner, I., Kofman, V., Kwabia–Tchana, F., Lavrentieva, N., Lee, T., Long, D., Lukashevskaya, A., Lyulin, O., Makhnev, V., Matt, W., Massie, S., Melosso, M., Mikhailenko, S., Mondelain, D., Müller, H., Naumenko, O., Perrin, A., Polyansky, O., Raddaoui, E., Raston, P., Reed, Z., Rey, M., Richard, C., Tóbiás, R., Sadiek, I., Schwenke, D., Starikova, E., Sung, K., Tamassia, F., Tashkun, S., Vander Auwera, J., Vasilenko, I., Vigasin, A., Villanueva, G., Vispoel, B., Wagner, G., Yachmenev, A., and Yurchenko, S. (2022). The hitran2020 molecular spectroscopic database. *Journal of Quantitative Spectroscopy and Radiative Transfer*, 277:107949.

Hedelt, P., von Paris, P., Godolt, M., Gebauer, S., Grenfell, J. L., Rauer, H., Schreier, F., Selsis, F., and Trautmann, T. (2013). Spectral features of Earth-like planets and their detectability at different orbital distances around F, G, and K-type stars. , 553:A9.

Igel, A. L. and van den Heever, S. C. (2017a). The importance of the shape of cloud droplet size distributions in shallow cumulus clouds. part i: Bin microphysics simulations. *Journal of the Atmospheric Sciences*, 74(1):249 – 258.

Igel, A. L. and van den Heever, S. C. (2017b). The importance of the shape of cloud droplet size distributions in shallow cumulus clouds. part ii: Bulk microphysics simulations. *Journal of the Atmospheric Sciences*, 74(1):259 – 273.

Karman, T., Gordon, I. E., van der Avoird, A., Baranov, Y. I., Boulet, C., Drouin, B. J., Groenenboom, G. C., Gustafsson, M., Hartmann, J.-M., Kurucz, R. L., Rothman, L. S., Sun, K., Sung, K., Thalman, R., Tran, H., Wishnow, E. H., Wordsworth, R., Vigasin, A. A., Volkamer, R., and van der Zande, W. J. (2019). Update of the HITRAN collision-induced absorption section. , 328:160–175.

Kasting, J. F., Whitmire, D. P., and Reynolds, R. T. (1993). Habitable zones around main sequence stars. *Icarus*, 101(1):108–128.

Kofman, V. and Villanueva, G. L. (2021). Absorption in exoplanet atmospheres: Combining experimental and theoretical databases to facilitate calculations of the molecular opacities of water. *Journal of Quantitative Spectroscopy and Radiative Transfer*, 270:107708.

Komacek, T. D. and Abbot, D. S. (2019). The atmospheric circulation and climate of terrestrial planets orbiting sun-like and m dwarf stars over a broad range of planetary parameters. *The Astrophysical Journal*, 871(2):245.

Kopparapu, R. K., Ramirez, R., Kasting, J. F., Eymet, V., Robinson, T. D., Mahadevan, S., Terrien, R. C., Goldman, S. D., Meadows, V., and Deshpande, R. (2013). Habitable zones around main-sequence stars: New estimates. *The Astrophysical Journal*, 765(2):131.

Kopparapu, R. K., Wolf, E. T., Arney, G., Batalha, N. E., Haqq-Misra, J., Grimm, S. L., and Heng, K. (2017). Habitable moist atmospheres on terrestrial planets near the inner edge of the habitable zone around m dwarfs. *The Astrophysical Journal*, 845(1):5.

Kossakowski, D., Kürster, M., Trifonov, T., Henning, T., Kemmer, J., Caballero, J. A., Burn, R., Sabotta, S., Crouse, J. S., Fauchez, T. J., Nagel, E., Kaminski, A., Herrero, E., Rodrí guez, E., González-Álvarez, E., Quirrenbach, A., Amado, P. J., Ribas, I., Reiners, A., Aceituno, J., Béjar, V. J. S., Baroch, D., Bastelberger, S. T., Chaturvedi, P., Cifuentes, C., Dreizler, S., Jeffers, S. V., Kopparapu, R., Lafarga, M., López-González, M. J., Martín-Ruiz, S., Montes, D., Morales, J. C., Pallé, E., Pavlov, A., Pedraz, S., Perdelwitz, V., Pérez-Torres, M., Perger, M., Reffert, S., López, C. R., Schlecker, M., Schöfer, P., Schweitzer, A., Shan, Y., Shields, A., Stock, S., Wolf, E., Osorio, M. R. Z., and Zechmeister, M. (2023). The CARMENES search for exoplanets around m dwarfs. *Astronomy &amp Astrophysics*, 670:A84.

Krissansen-Totton, J., Schwieterman, E. W., Charnay, B., Arney, G., Robinson, T. D., Meadows, V., and Catling, D. C. (2016). Is the pale blue dot unique? optimized photometric bands for identifying earth-like exoplanets. *The Astrophysical Journal*, 817(1):31.

Linsenmeier, M., Pascale, S., and Lucarini, V. (2015). Climate of earth-like planets with high obliquity and eccentric orbits: Implications for habitability conditions. *Planetary and Space Science*, 105:43–59.

Mandell, A. M., Lustig-Yaeger, J., Stevenson, K. B., and Staguhn, J. (2022). Mirecle: Science yield for a mid-infrared explorer-class mission to study nontransiting rocky planets orbiting the nearest m stars using planetary infrared excess. *The Astronomical Journal*, 164(5):176.

Massie, S. T. and Hervig, M. (2013). HITRAN 2012 refractive indices. , 130:373–380.

Mlawer, E. J., Payne, V. H., Moncet, J.-L., Delamere, J. S., Alvarado, M. J., and Tobin, D. C. (2012). Development and recent evaluation of the mt_ckd model of continuum absorption. *Philosophical Transactions of the Royal Society A: Mathematical, Physical and Engineering Sciences*, 370(1968):2520–2556.

Nowajewski, P., Rojas, M., Rojo, P., and Kimeswenger, S. (2018). Atmospheric dynamics and habitability range in earth-like aquaplanets obliquity simulations. *Icarus*, 305.

Ozaki, K., Cole, D. B., Reinhard, C. T., and Tajika, E. (2022). Canops-grb v1.0: a new earth system model for simulating the evolution of ocean–atmosphere chemistry over geologic timescales. *Geoscientific Model Development*, 15(20):7593–7639.

Paradise, A., Macdonald, E., Menou, K., Lee, C., and Fan, B. L. (2022). ExoPlaSim: Extending the Planet Simulator for exoplanets. , 511(3):3272–3303.

Robock, A. (1980). The seasonal cycle of snow cover, sea ice and surface albedo. *Monthly Weather Review*, 108(3):267 – 285.

Rondanelli, R. and Lindzen, R. (2010). Can thin cirrus clouds in the tropics provide a solution to the faint young sun paradox? *Journal of Geophysical Research*, 115.

Salamah, U., Sakti, S. P., Soetedjo, H., and Naba, A. (2022). Non-contact technique for co2 gas monitoring using thermal imaging camera. *Journal of Physics: Conference Series*, 2165(1):012019.

Seager, S. (2014). The future of spectroscopic life detection on exoplanets. *Proceedings of the National Academy of Sciences*, 111(35):12634–12640.

Segura, A., Kasting, J. F., Meadows, V., Cohen, M., Scalo, J., Crisp, D., Butler, R. A., and Tinetti, G. (2005). Biosignatures from earth-like planets around m dwarfs. *Astrobiology*, 5(6):706–725.

Smith, A. J. R. W., Katherina Feng, Y., Fortney, J. J., Robinson, T. D., Marley, M. S., Lupu, R. E., and Lewis, N. K. (2020). Detecting and characterizing water vapor in the atmospheres of earth analogs through observation of the 0.94 m feature in reflected light. *The Astronomical Journal*, 159(2):36.

Stull, R. (2011). Wet-bulb temperature from relative humidity and air temperature. *Journal of Applied Meteorology and Climatology*, 50(11):2267 – 2269.

Suissa, G., Wolf, E. T., kumar Kopparapu, R., Villanueva, G. L., Fauchez, T., Mandell, A. M., Arney, G., Gilbert, E. A., Schlieder, J. E., Barclay, T., Quintana, E. V., Lopez, E., Rodriguez, J. E., and Vanderburg, A. (2020). The first habitable-zone earth-sized planet from tess. iii. climate states and characterization prospects for toi-700 d. *The Astronomical Journal*, 160(3):118.

Villanueva, G. L., Liuzzi, G., Faggi, S., Protopapa, S., Kofman, V., Fauchez,

T., Stone, S. W., and Mandell, A. M. (2022). *Fundamentals of the Planetary Spectrum Generator*.

Villanueva, G. L., Smith, M. D., Protopapa, S., Faggi, S., and Mandell, A. M. (2018). Planetary Spectrum Generator: An accurate online radiative transfer suite for atmospheres, comets, small bodies and exoplanets. , 217:86–104.

Wallace, J. and Hobbs, P. (2006). *Atmospheric Science: An Introductory Survey*. International Geophysics Series. Elsevier Academic Press.

Wunderlich, Fabian, Godolt, Mareike, Grenfell, John Lee, Städt, Steffen, Smith, Alexis M. S., Gebauer, Stefanie, Schreier, Franz, Hedelt, Pascal, and Rauer, Heike (2019). Detectability of atmospheric features of earth-like planets in the habitable zone around m dwarfs. *A&A*, 624:A49.

Yang, J., Hammond, M., Piette, A. A. A., Blecic, J., Bell, T. J., Irwin, P. G. J., Parmentier, V., Tsai, S.-M., Barstow, J. K., Crouzet, N., Kreidberg, L., Mendonça, J. M., Taylor, J., Baeyens, R., Ohno, K., Teinturier, L., and Nixon, M. C. (2024). Simultaneous retrieval of orbital phase resolved jwst/miri emission spectra of the hot jupiter wasp-43b: evidence of water, ammonia and carbon monoxide.

Appendix A

Appendix

A1 Table appendix

Parameter	Description	Value
Object		
Phase	Angular parameter (season/phase) that defines the position of the planet moving along its Keplerian orbit. For exoplanets, 0:Secondary transit, 180:Primary transit, 90/270:Opposition.	90^o
Velocity	Relative velocity between the observer and the object	0.0 km/s
Inclination	Orbital inclination [degree], mainly relevant for exoplanets. Zero is phase on, 90 is a transiting orbit	90^o
Solar latitude	Sub-solar latitude [degree]. Parameter related with obliquity	Obliquity of each aquaplanet
Stellar radius	Radius of the host star measured in Sun radii	1 R_{sun}
Stellar metallicity	Metallicity of the host star and object with respect to the Sun in log [dex]	0.0
Stellar velocity	Velocity of the planet to the Sun [km/s], and for exoplanets the RV amplitude [km/s]	0.0 km/s
Geometry		
Type	Type of observing geometry	Observatory

Observation altitude	Distance between the observer and the surface of the planet	1 Pc
Stellar magnitude	For stellar occultations, this field indicates the brightness [magnitude] of the occultation star	0
Generator		
Instrument	Instrument which will observe the object for the simulation	JWST
Telescope	Type of telescope	Single dish
Telescope diameter	Diameter of the main reflecting surface of the telescope or instrument	5.64 m
Spectral range	Spectral range for the simulation	$0.3 - 30$ μm
Resolution	Spectral resolution for the simulation in RP: 'Resolving power' unit	100
Noise	Identifying the noise model to consider	No
Beam	Full width half-maximum (FWHM) of the instrument's beam or field-of-view (FOV). Measured in diffrac:'defined by the telescope diameter and center wavelength	1.0
GCM binning	Spatial binning applied to the GCM data when computing spectra. 1: Full resolution	5

Surface		
Model	Type of scattering model describing the surface	Lambert
Albedo	Albedo the surface [0:non-reflectance, 1:fully-reflective]	0.06
Atmosphere		
Structure	The structure of the atmosphere	Equilibrium
Gas	Name of the gases to include in the simulation	N2, CO2, H2O
Gas abundance	Abundance of gases. The values can be assumed to be same across all altitudes/layers and measured in [%] for N2 and CO2. In the case of H2O is provided by vertical profile of the GCM	96.5 %, 3.5 %, GCM
Spectral type	Spectral database sub-type which will compute the spectra	HIT[22],HIT[2],HIT[1]
Aerosol	Name of the aerosols to include in the simulation. This is only included for the cloudy case spectra simulation.	Water
Aerosol abundance	Abundance of gases. In this case is provided by vertical profile of the GCM	GCM

Aerosol spectral type	Spectral database sub-type of the aerosols	AFCRL_Water_HRI
Aerosol particle size	Effective radius of the aerosol particles. The values is assumed to be same across all layers, latitude and longitude	0.5 μm
Processes	Continuum processes to be included in the calculation	Rayleigh,Refraction, CIA_all,UV_all
Layers	Number of layers of the atmospheric vertical profile	10
GCM parameters	Parameters defining the 3D General Circulation Model grid.	Eastward and northward wind, T_A, T_S, Albedo, Pressure, q, Water content in clouds
NMAX	When performing scattering aerosols calculations, this parameter indicates the number of n-stream pairs	4

LMAX	When performing scattering aerosols calculations, this parameter indicates the number of scattering Legendre polynomials used for describing the phase function	60

Table A1.1: Aquaplanet parameters used for simulation of emission spectrum of the Archean Earth-like with varying obliquity model. This is the configuration used with PSG.

A2 Figures appendix

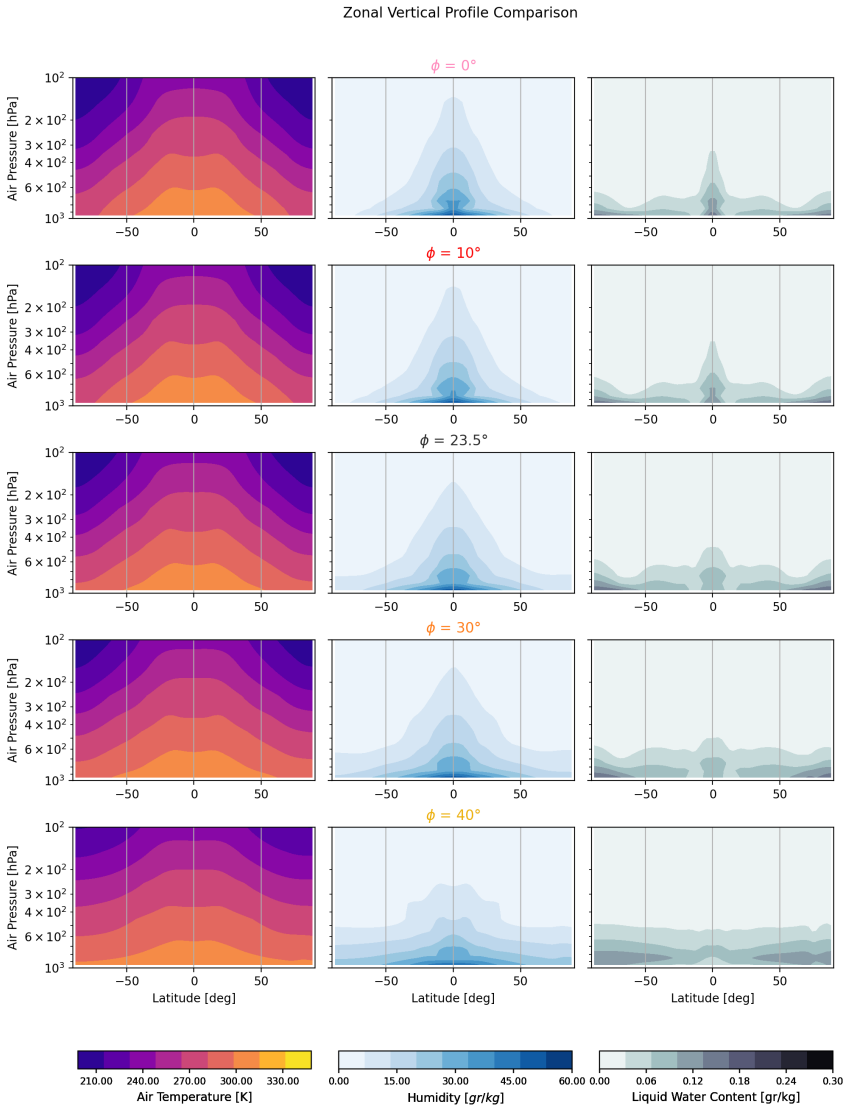

Figure A2.1: Comparison of annual zonal vertical profiles of **(a)** Air temperature, **(b)** Specific humidity, and **(c)** Liquid water content in clouds of Archean Earth-like aquaplanets. Each row represents the cases with $\phi = 0^o, 10^o, 23.5^o, 30^o, 40^o$ with their respective colors. Notable differences in water content between gaseous and liquid phases are observed between the simulations.

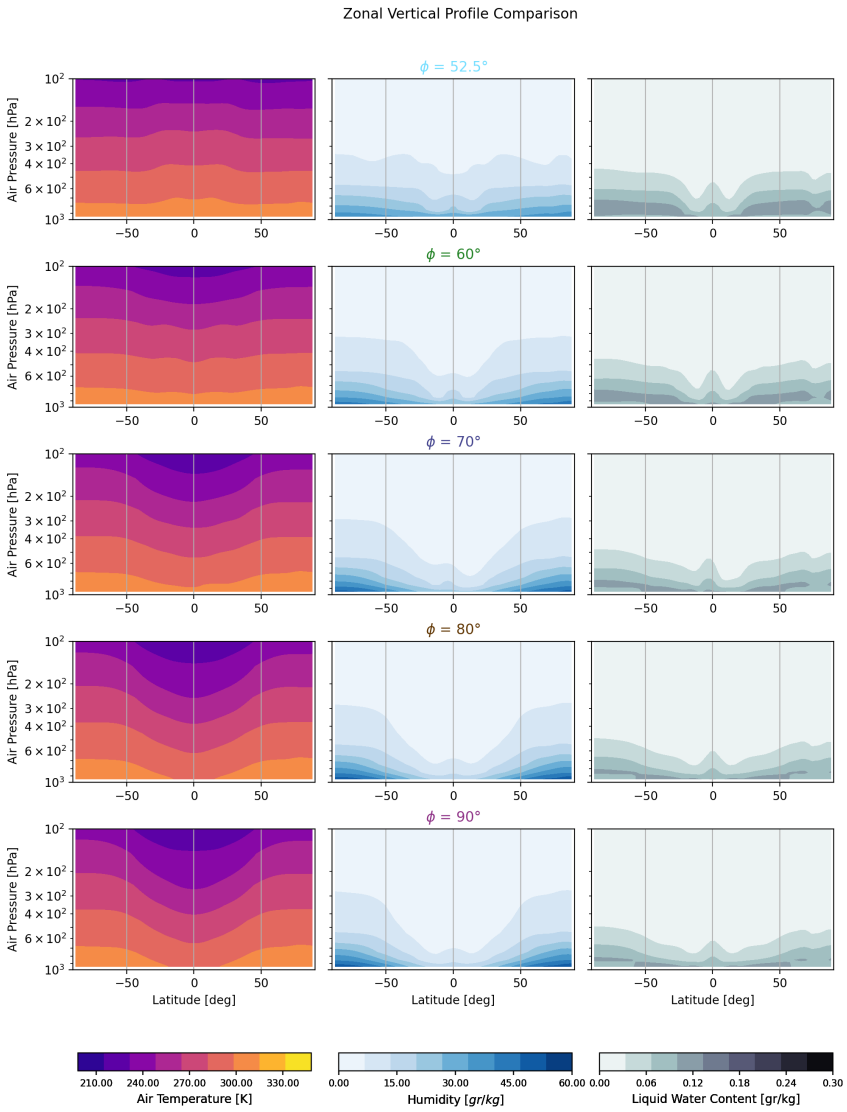

Figure A2.2: Comparison of annual zonal vertical profiles of **(a)** Air temperature, **(b)** Specific humidity, and **(c)** Liquid water content in clouds of Archean Earth-like aquaplanets. Each row represents the cases with $\phi = 52.5^o, 60^o, 70^o, 80^o, 90^o$ with their respective colors. Notable differences in water content between gaseous and liquid phases are observed between the simulations.

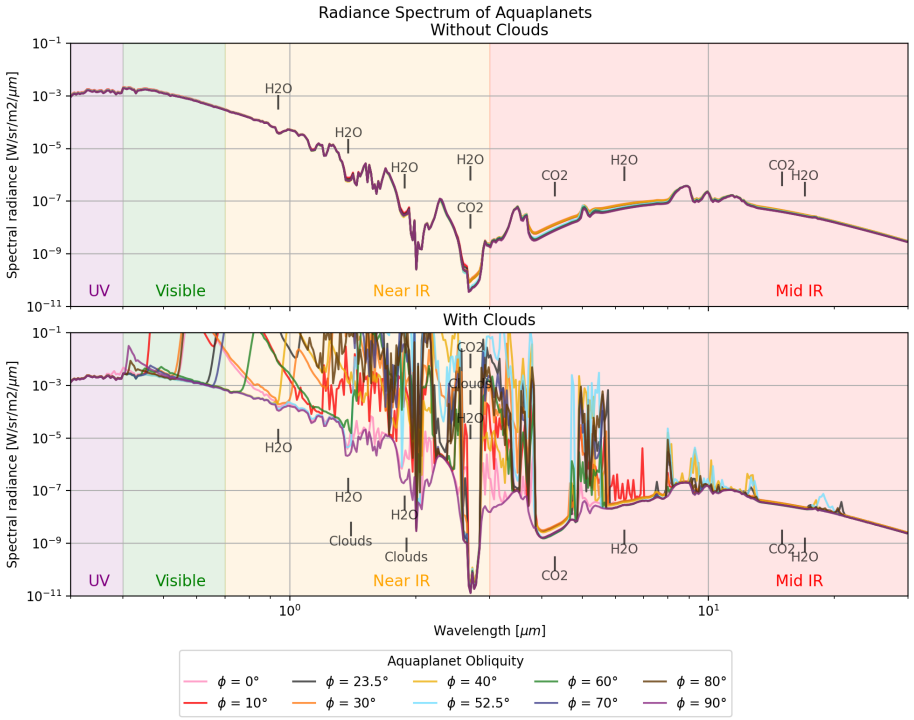

Figure A2.3: Radiation spectrum of all simulated aquaplanets. The **upper panel** shows the spectrum without the observational effect of clouds. The **bottom panel** includes the observational effect of clouds. The purple/green/orange/orange/red colored background represents the UV/Visible/NIR/MidIR bands of the electromagnetic spectrum. Labeled are the absorption lines of H_2O, CO_2 and Clouds. The spectrum shows both reflected and emitted light from aquaplanets.

Appendix B

Statement on the Use of AI Assistance

In this work, artificial intelligence (AI) assistance provided by the ChatGPT platform from OpenAI has been used to enhance the cohesion and clarity of the text. Specifically, AI was employed for drafting and editing sections to ensure better flow and coherence in the presentation of the content.

It is important to note that AI was not used for the interpretation of results or the generation of scientific conclusions. All analyses, interpretations, and conclusions presented in this document have been performed and verified by human researchers. The final text has been thoroughly reviewed and approved by the authors to ensure the accuracy and integrity of the content.